

High dynamic range dual-modal white light imaging system improves the accuracy of tumor bed sampling after neoadjuvant therapy for breast cancer

Yueping Liu (✉ annama@163.com)

The Fourth Hospital of Hebei Medical University

Jianhua Yao

Tencent

Hong Bu

West China Medical Center of Sichuan University

Meng Zhang

The Fourth Hospital of Hebei Medical University

Jun Liao

Tencent

Zhanli Jia

The Fourth Hospital of Hebei Medical University

Chenchen Qin

Tencent

Lingling Zhang

The Fourth Hospital of Hebei Medical University

Han Wang

Tencent

Yao Liu

The Fourth Hospital of Hebei Medical University

Cheng Jiang

Tencent

Mengxue Han

The Fourth Hospital of Hebei Medical University

Jinze Li

The Fourth Hospital of Hebei Medical University

Kun Wang

The Fourth Hospital of Hebei Medical University

Xinran Wang

The Fourth Hospital of Hebei Medical University

Research Article

Keywords: HDWIS, tumor bed, sample, transmittance, reflection image, visual observation

Posted Date: April 13th, 2022

DOI: <https://doi.org/10.21203/rs.3.rs-1535293/v1>

License:  This work is licensed under a Creative Commons Attribution 4.0 International License.

[Read Full License](#)

Abstract

Background

Accurate evaluation of residual cancer burden (RCB) remains challenging due to the lack of appropriate techniques for tumor bed sampling. Therefore, this study evaluated the application of white light imaging system in assisting pathologists differentiating the components and location of tumor bed in specimens.

Methods

The high dynamic range dual-mode white light imaging system (HDWIS) was developed to capture anti-glare reflection and high dynamic range (HDR) transmission images and was tested in sixty specimens of modified radical mastectomy after neoadjuvant therapy. We observed the differential transmittance among tumor tissue, fibrosis tissue and adipose tissue. The sensitivity and specificity of HDWIS were compared with x-ray or visual examination to determine whether HDWIS was superior in identifying tumor beds.

Results

We found tumor tissues had lower transmittance (0.12 ± 0.03) than fibers (0.15 ± 0.04) and fats (0.27 ± 0.07) ($P < 0.01$). HDWIS was more sensitive in identifying fiber and tumor tissues than cabinet X-ray and visual observation ($P < 0.01$). In addition, HDWIS could identify more fibrosis areas than the currently used Whole Slide Imaging (WSI) did in 12 samples (12/60).

Conclusions

We have determined that HDWIS can provide more in-depth tumor bed information than X-ray and visual examination do, which will help prevent the diagnostic error in tumor bed sampling.

1. Background

With the increasing demand of neoadjuvant therapy for breast cancer patients, the accurate pathological evaluation of tumor bed is critical for the selection of treatment options and the prediction of the prognosis[1–3]. Breast International Group- North American Breast Cancer Group (BIG-NABCG) strongly recommends the use of residual cancer burden (RCB) statistics to evaluate the tumor bed[4, 5]. Although RCB has more prognostic value than other evaluation systems, it is still suboptimal. Obtaining the largest cross-section of tumor bed is essential for the final RCB grading, especially when the lymph node contribution is minimal (the metastasis is minimal or there is no positive lymph node) [6–8]. Therefore, pathologists are required to accurately identify the largest cross-section of the tumor bed without missing small lesions for RCB evaluation[9]. However, visual examination could give human errors, and the

pathologists may not be able to distinguish normal fibers from tumor tissues due to their similarity in color, which prevents them from sampling the largest cross-section of the tumor bed for subsequent RCB evaluation.

At present, only few imaging techniques are available to assist specimen sampling; thus, most pathologists still rely on their personal experience and intuition to estimate the tumor bed [10, 11]. The development of the cabinet X-ray imaging system has simplified the specimen sampling [12, 13]. Pathologists can distinguish dense tissues such as tumors from adipose tissue based on X-ray image. However, differentiating tumor tissues from fiber tissues is challenging because both give similar gray colors on X-ray image. Moreover, X-ray machines are expensive and emit ionizing radiation. To overcome these obstacles, other imaging techniques such as ultrasound [14, 15], hyperspectral imaging [16–18], fluorescence multispectral imaging [19–21], and terahertz imaging [22–24] have been proposed for breast cancer intraoperative tumor margin evaluation. Nonetheless, these techniques are costly, and most of them require professional technicians to operate the systems and to interpret the imaging results [25–27]. Thus, an easy to operate, safe, and cost-effective specimen sampling technique is urgently needed.

Herein, we developed a high dynamic range dual-mode white light imaging system (HDWIS) for specimen sampling. This system was equipped with white LED light source and could capture the reflection and transmission images of the specimen. Moreover, polarized reflection illumination was used to remove the glare from reflective surfaces. Transmission images with multiple exposure times were captured to compose the high dynamic range (HDR) image. By doing this, information from inside and outside of tumors were collected to assist specimen sampling. Compared to the cabinet X-ray and visual observation, HDWIS is more accurate in identifying the adipose tissues, normal fibers, and tumors, as well as in determining the largest cross-section of tumor bed for thick specimens. With these advantages, HDWIS offers a more useful auxiliary sampling technique.

2. Methods

2.1 Selection of samples

Sixty specimens of modified radical mastectomies after neoadjuvant chemotherapy were selected, and all cases were from the Fourth Hospital of Hebei Medical University from November 2020 to April 2021 and met the following criteria: suspicious fibrosis or tumor visible from the surface, and samples excised beyond roughly 2 cm of the tumor margin. Specimens suspected of occult breast cancer before neoadjuvant therapy were excluded.

To determine the effect of tissue thickness on transmittance, 36 tissues of various thickness, 3 mm, 5 mm, and 7 mm, were collected. Each thickness group contained four samples of three tissue types: tumors, fibers, and fats. The area of each sample was approximately 15–20 mm × 10–15 mm, and the samples were arranged in a 3×4 matrix for a transmittance test.

2.2 Sample information

Sixty patients at 42–69 (median 55) years old were enrolled. The preoperative tumor size determined by radiology was 2.5–7 cm, with a median size of 5 cm. According to core needle biopsy, 47 cases were diagnosed as breast invasive ductal carcinoma (IDC) grade II, 12 cases as IDC grade III, and 1 case as mucinous carcinoma. Among IDC II patients, 15 cases had different grades of ductal carcinoma *in situ*, [DCIS]. Additionally, 55 of these 60 patients had axillary lymph node metastasis. After 3–8 cycles of neoadjuvant therapy, 35 cases had residual tumors determined by gross specimen evaluations, including 18 cases with significant reduction of tumor bed size (2–3 cm), 8 cases with no obvious size change (3–4.5 cm), and 9 cases with microcalcification only.

The histology diagnosis after surgery confirmed 41 cases of carcinoma including 36 cases of IDC (28 cases of grade II and 8 cases of grade III), 5 cases of DCIS, and 19 cases without cancer cells (6 cases showed minimal inflammatory cell exudation, 10 cases showed necrosis, and 3 exhibited a number of multinucleated cells and foam cells with few inflammatory cells). 2 out of 28 IDC grad II are mixed with DCIS. 4 out of 8 IDC grad III are mixed with DCIS.

2.3 Experimental instrument and platform

The cabinet X-ray system was the Bio Vision system by Faxitron (American). Canon color camera (Japan) was used to capture the color images of the specimens.

2.4 HDWIS

Figure 1A is the schematic diagram of HDWIS. The capture box was made of black matte opaque acrylic. Two white bar LED light bars (10 W each) were first installed on the top surface inside the capture box as the reflection illumination source. Next, we installed polarizing films (400–700 nm, extinction ratio 97%) with the same polarization direction on the surface of both light sources. A white square LED light (24 W) was installed at the bottom center of the capture box as a backlight. Moreover, we used a power controller to adjust the power of all the light sources in the capture box. Finally, an auto-focus camera with a built-in micro-motor for sensor movement was placed on the upper part of the capture box (Shunli C304 industrial camera with a resolution of 4000 × 3000). The zoom lens was a Canon EF-S 18–55 mm F/3.5–5.6 IS II SLR, and a circular polarizing filter (CPL) was installed on the surface of the lens. To remove the glare from reflection lights, the polarizer on the lens was set perpendicularly to the polarizers in front of the bar LEDs. A transparent acrylic plate was used as a sample tray.

As shown in Fig. 1B, for each specimen, HDWIS generated one reflection image and five transmission images of multiple exposures (at intervals of 1/30 s, 1/50 s, 1/100 s, 1/200 s, and 1/250 s). These transmission images were then used to compose an HDR transmission image to expand the scale of contrast and color. Compared with pictures by Canon camera, HDWIS possesses three specific functions as shown in Fig. 1C: anti-glaring, optical zooming, and HDR transmission.

2.5 Study plan

Figure 1D–F showed our general study plan. According to the recommendations by BIG-NABCG collaboration[28], the breast tumor specimens were dissected and then fixed with 10% formalin (Fig. 1D).

Tissue sampling of 6.5-7 mm thickness was carried out by pachymeter. To evaluate the effectiveness of HDWIS in specimen sampling, we compared it with two conventional methods: Visual examination (recorded by a color camera) and X-ray imaging (Fig. 1E). A matrix of the tissue samples in the 3-, 5-, and 7-mm thickness groups was employed to test the transmittance of HDWIS, and the selected regions of interest according to the WSI were applied for transmittance calculation (Fig. 3).

Three pathologists evaluated the tissue types by these three methods. There was a one-week gap between using X-rays and HDWIS images. Finally, we compared the results with the virtual large slides stitched by WSI fragments (Fig. 1f), the gold standard to calculate the sensitivity and specificity of each method. We used the nonparametric rank-sum test method of multiple paired samples to compare the specificity and sensitivity of different methods.

The pathologists enrolled in this study have at least 3 years of clinical experience and are all trained with the following labeling standards: For visual observation method, the standards come from the book [29] (WHO Classification of Tumours, 5th Edition, Volume 2), which is regarded as the gold standard for the diagnosis of breast tumors. Grossly, the adipose is yellow. The fibrous tissue looks white and is usually not rough and has a regular texture. The cancer tissue is generally off-white, darker than fibrous tissue, and looks rough in texture. Cancer generally has irregular, stellate outline or nodular configuration. As the book admitted that the cancer edge is usually moderately or poorly defined and lacks sharp circumscription. For X-ray method, the contrast is generated by the tissue density. Dense tissue such as cancer and fiber look white on X-ray images. Adipose tissue looks darker than cancer and fiber. Differentiating cancer and fibrous tissue can be difficult as they have close intensity on X-ray images. For HDWIS, from the transmission image, first, we differentiate three types of tissue by their transmittance difference (transmittance: Adipose > fiber > cancer). Second, we can observe different tissue textures in the transmission image: Fiber has regular textures such as linear texture, cancer is irregular. For the reflection image, the rules are the same as that of the visual method above.

3. Results

3.1 HDWIS's transmission image helps identify tissue types through contrast difference.

Utilizing HDWIS to capture the specimen, we found that the transmission images contained more information to aid pathologists in differentiating tumors and fibrosis areas with more confidence (Fig. 2A1-C3). Specifically, in the HDR transmission images, the tumor areas were the darkest among tumors, fibers, and fats. Confirmed by the WSIs, the otherwise "invisible" tumor in the reflection images and larger fiber areas were observed in the transmission images. And we also calculated the average transmittance of the fat, fiber, and tumors, as seen in the yellow, green, and red boxes, respectively in Fig. 2B1-B3. Fat tissues had the highest transmittance followed by fiber and tumor.

We next analyzed the transmittance of the tumors, fibers and fats of all 60 samples by calculating the brightness according to each pixel. Figure 2D showed the average brightness of these three tissue types. Additionally, we used the transmittance results for each color channel (red, green, and blue) to obtain color images. As shown in Fig. 2D, the light intensity was in grayscale by converting the color image to a gray image. The relative transmittance values was calculated into a scale from 0–1 with 1 indicating the background brightness or the transmittance of the air. For specimens with a thickness of 6.5-7 mm, we found that tumors had significantly lower transmittance (0.12 ± 0.03) ($P < 0.01$) than fibers (0.15 ± 0.04) and fats (0.27 ± 0.07) did.

Furthermore, we found that the sample thickness had no effect on its transmittance. In addition, among tumor, fat and fiber tissues, the matrix calculation indicated that tumor had the lowest transmittance in all thickness (3, 5, and 7 mm) samples (3 mm tumors: 0.20 ± 0.02 , fibers: 0.28 ± 0.03 , and fats: 0.42 ± 0.04 , $P \leq 0.01$; 5 mm tumors: 0.15 ± 0.03 , fibers: 0.22 ± 0.02 , and fats: 0.27 ± 0.03 , $P \leq 0.05$; 7 mm tumors: 0.08 ± 0.01 , fibers: 0.18 ± 0.01 , and fats: 0.27 ± 0.04 , $P \leq 0.01$) (Fig. 3). Furthermore, as the thickness increased, the light intensity of the tumor, fiber, and fat areas decreased (Fig. 3B). These results suggested that the transmittance data could be used to distinguish fats, fibers, and tumors in different channels of transmittance (Fig. 3C).

3.2 The texture features in the transmission image helped identify tissue types.

In addition to transmittance difference, we also determined if the texture features in transmission images would help pathologists to identify tissue types. We detected the directional textures in fibrosis areas in 50 out of the 60 specimens and non-directional textures in the tumor areas in all 41 tumor samples. We observed directional textures in fibrosis areas, as indicated by the green box in Fig. 4, while tumor areas exhibited disordered or non-directional textures as indicated by the red box. The same pattern was observed in WSI images.

3.3 Combining the reflection and the transmission images to identify tissue types

Based on the above observation, we could use the difference in transmittance and the texture features to identify tissue types. However, we found 11 cases with misleading transmission contrast and textures (Fig. 5A). The areas indicated by the black arrows in the transmission image presented low transmittance. In the reflection image, these suspicious areas were yellow on the surface. We suspected that these areas might be mixed with fats and fibers, which was subsequently confirmed by WSI. Figure 5 also showed the X-ray images of the specimens, which displayed high contrast between fat and non-fat areas, but low contrasts between fibrosis and tumor areas, suggesting that fibrosis and tumor areas exhibited close absorption scales within the X-ray range (single channel: 0.01-10 nm) but were distinguishable between RGB channels (three channels: 400–700 nm).

3.4 Comparison on the ability of different methods to detect tumor bed

Through pixel-wise statistical analysis in the identified fields, we calculated the sensitivity and specificity of HDWIS, X-ray imaging, and visual observation for fibrosis and tumor areas. Figure 6A-B showed that HDWIS had the highest sensitivity for both fibrosis and tumors (82.7% and 41%, respectively) compared to X-ray (69.2% and 35.4%, respectively) and visual examination (64.2% and 32.1%, respectively; fibers: $P \leq 0.001$; tumors $P \leq 0.01$). But these three approaches failed to demonstrate statistical significance in specificity level (fibers: HDWIS: 87.3%, X-ray: 93.4%, and visual observation: 92.6%; tumors: HDWIS: 71.6%, X-ray: 64.8%, and visual observation: 69.3%). As there are hard cases and easy cases, the difficulty of correct cancer margin assessment varies. However, the cancer sensitivity of HDWIS outperforms the visual method among most samples. Therefore, a small p-value and a large error bar in Fig. 6B are not contradictory.

Figure 6A showed that the specificity of HDWIS for fibrosis areas was slightly lower than that of the other two methods. If using the commonly accepted 2D WSI as the reference, HDWIS seemed to mistakenly identify non-fiber parts as fibers. However, since large virtual slides stitched by WSI fragments included only one cross-section of the specimen, the 2D WSI result might not represent the features of the entire tumor. Thus, we believed that 3D WSI was more suitable as the gold standard than 2D WSI. To prove this, we conducted the experiments below.

3.5 HDWIS could reveal a more complete tumor bed range

In 12 out of the 60 specimens, the HDWIS transmission images showed a larger range of fibrosis areas than the 2D WSI; two of the representative samples were shown in Fig. 6C1-H2. To determine if larger fibrosis areas also presented in other sections of the specimen, we sliced the paraffin-embedded sample in 20 μm interval to cover more areas in order to identify the section with the largest scope of fiber. And the identified cross-section was used to make a deep WSI, rather than a surface WSI which was determined in the first section of the sample. As shown in Fig. 6G1 and G2, the deep WSI revealed the cross-section with the maximum fibrosis area, and the fibrosis area in the deep WSI cross-section closely matched the findings from the HDWIS transmission images. As shown in the reflection images (Fig. 6C1 and C2), visual observation might not provide the complete picture of tumor bed information. Similarly, X-ray images in Fig. 6E1 and E2 also showed smaller fibrosis areas than the deep WSI did (Fig. 6G1 and G2).

The above findings prompted us to reevaluate the tumor bed in those 12 specimens examined by deep WSI, and we found that the fiber sensitivity of HDWIS was even higher by 3.7% (before: 90%, after: 93.7%), while the sensitivity of X-ray imaging decreased by 14.5% (before: 70.5%, after: 56%). The sensitivity of visual observation decreased by 15.5% (before: 69.2%, after: 53.7%) (Fig. 6I). Importantly, the fiber specificity of HDWIS increased by 18.4% (before: 74.5%, after: 92.9%, $P < 0.05$) (Fig. 6J), in contrast to the result in Fig. 6A where HDWIS had low specificity for fiber. Therefore, we concluded that the transmission

images of the HDWIS performed well in determining the largest cross-sectional areas of a specimen with 6.5-7 mm thickness, especially for those samples with a larger fiber portion inside the specimen than on the surface.

4. Discussion

The pathological evaluation of breast cancer after neoadjuvant therapy requires accurate specimen sampling so that essential information can be obtained to measure the maximum diameter for RCB assessment. This evaluation system contains 6 elementary factors including two maximum diameters of the largest cross-section of tumor bed, overall cancer cellularity, percentage of cancer area, number of positive lymph nodes, and diameter of largest metastasis. A precise sampling of the largest cross-section will enable us to gain accurate data on four elements. Thus, the current standard for RCB evaluation requires pathologists to accurately identify the various tissue types, e.g., tumors, fibers, fats, in the tumor bed[30, 31] .

Conventional methods of specimen sampling mainly rely on visual observation, and the conclusion is mostly based on experience. For example, we consider gray-yellow areas as fat, gray areas as fiber, and gray-white areas as tumor. However, the carcinoma is very heterogenous; hence these evaluation are subjective. Traditional methods also include touching to estimate the sample's texture, which has poor reproducibility. Moreover, lesions inside the specimen are not visible by eyes. If the pathologist fails to accurately determine the distribution of tumors, there are at least two severe consequences: the blind sampling, which results in an increased workload, and a damage to the tumor bed of the largest cross-section and a reduced accuracy. Other methods such as X-ray imaging have been used, but they are expensive with ionizing radiation and not showing high contrasts among fats, fibers, and tumors.

In recent years, advancement in technologies has improved the clinical diagnosis. For instance, hyperspectral and multispectral provide certain resolution to human tissues[32–37], and radiation can be replaced by visible light (400-700nm) in some area[38–40]. Significantly, we developed the high dynamic range dual-modal white light imaging system for tumor bed sampling.

The HDWIS system we designed contains three primary techniques: transmissive imaging, polarized imaging, and high dynamic range (HDR) imaging, which are already widely used in photography, industrial inspection, and certain medical fields. For example, transmissive imaging is used for egg sorting and grading [41]. Polarized imaging is widely used for industrial material classification [42] and skin examination [43]. HDR [44] is also a popular technology in the field of photography and exists in almost all current DSLR cameras and mobile phones to expand the range of both contrast and color of the image.

The HDWIS imaging system is able to produce anti-glaring reflection and HDR transmission specimen images and provide pathologists with information not only from surface but also inside the specimen. The multi-exposure transmission images are also particularly important when the tumor beds have larger thickness value. Based on the difference in transmittance, we can distinguish tissue types such as

tumors, fibers, and fats. Although the transmittance of all tissue types declines with increasing thickness, there is no linear correlation between thickness and transmittance as shown in Fig. 3B, suggesting that the transmittance of tissue is affected not only by the thickness but also by the characteristics/texture of the tissues. By combining the transmittance information and the texture features of the transmission images, we might identify the locations of fibers, tumors, and fats more confidently.

In the transmission images by HDWIS, the fibrosis areas of the tumor beds displayed directional texture in 61% of the cases, while the textures of tumor areas were disordered, non-directional or invisible. Under the microscope, we observed that the fibroblasts displayed directional arrangement, while cancer cells were irregular (solid, sieve, or scattered). These micro-distribution patterns determined the tissue appearance and types, which displayed clear boundaries in the transmission images due to the differences in transmittance. The HDWIS reflection images are also important in this analysis. HDWIS with anti-reflection and ultra-fine focal-length-change function could further improve the assessment accuracy. The anti-reflection function could assist us in avoiding the omission of granular areas (DCIS), and the high-resolution camera could enlarge the texture images of small lesions for easy visual identification. However, for resolving power (R.P.), reflection image with high resolution and the visual observation give similar results. When the fibers are formed by hyaline, the directional texture disappears. Moreover, if the cancer cells are scarce, and fibers account for a large proportion of the tumor bed, tumors and fibers could not be differentiated through transmission images. By combining information from tissue colors, textures, and zoomed-in details of anti-reflection images, we will be able to overcome the complexity caused by tumor heterogeneity.

HDWIS has the highest detection sensitivity for fibers and tumors compared to the traditional methods. The transmission imaging method can identify the largest tumor bed area of 3–7 mm. HDR can further expand the dynamic range of the transmission images and provide more colors and details in both bright and dark areas. Additionally, the HDR transmission images could help find the fibrosis areas which were hard to detect by other techniques including the original 2D WSI and X-ray. The deep WSI and recalculated specificity shown in Fig. 6C1-H2 confirmed our observation. Although the imaging principles of X-ray and transmitted light are similar, the radiation dose of the cabinet X-ray system is fixed such that some samples cannot be examined in detail. HDWIS solves this issue by relying on multiple exposure transmission images and the optimized synthetic HDRs. Hence, HDWIS is superior in examining thick specimens via showing the tumor bed deep inside the specimen.

Nevertheless, HDWIS may not work well for tumor beds with complex non-concentric contraction patterns[45–47] or small lesions that are only detectable by histological microscope. The study scope of this work is confined to excised breast cancer specimens. Future studies may extend to other cancer specimens. Although the collected specimens are formalin-fixed, future studies may also extend to fresh cancer specimens as well by using the proposed method as a potential intraoperative cancer margin assessment tool. In addition, the ability of HDWIS to identify necrosis, inflammation, and other components requires further investigation.

5. Conclusion

We have demonstrated the ability of HDWIS in identifying fats, fibers, and tumors, superior to the traditional specimen sampling techniques. HDWIS is sufficient for accurate specimen sampling. Moreover, this method provides the largest tumor bed cross-section, which prevents from sampling omission, as well as enhances the accuracy of the tumor bed evaluation for RCB.

Declarations

Authors' contributions

MZ and JL participated in the study design, analyzed experimental data, wrote and revised the manuscript.

JL built and improved HDWIS.

CCQ developed the ASAP and WSI stitching software.

ZLJ, LLZ, YL labeled the tissue types.

HW calculated the transmittance.

CJ calculated the specificity and sensitivity.

MXH, JZL, KW and XRW sampled the tumor beds.

YPL, JHY and HB guided the study design and revised the manuscript.

All authors read and approved the final version of the manuscript, including the authorship list.

Acknowledgements

We thank all pathologists and engineers who participated in the preparation and implementation of this study.

Ethics approval and consent to participate

This study was approved by the ethics committee of the Fourth Hospital of Hebei Medical University. Written informed consent was obtained from all of participants according to the study protocols.

Availability of data and materials

The datasets used during the current study are available from the corresponding author on reasonable request.

Conflict of interest

The authors declare no conflict of interest.

Funding

None.

References

1. Hortobagyi GN. Comprehensive management of locally advanced breast cancer. *Cancer*. 1990;**66**(6 Suppl):1387–91.
2. Han R, Regpala S, Slodkowska E, *et al*. Lack of Standardization in the Processing and Reporting of Post-Neoadjuvant Breast Cancer Specimens. *Arch Pathol Lab Med*. 2020;**144**(10):1262–70.
3. Bossuyt V. Processing and Reporting of Breast Specimens in the Neoadjuvant Setting. *Surg Pathol Clin*. 2018;**11**(1):213–30.
4. Campbell JI, Yau C, Krass P, *et al*. Comparison of residual cancer burden, American Joint Committee on Cancer staging and pathologic complete response in breast cancer after neoadjuvant chemotherapy: results from the I-SPY 1 TRIAL (CALGB 150007/150012; ACRIN 6657). *Breast Cancer Res Treat*. 2017;**165**(1):181–91.
5. Bossuyt V, Provenzano E, Symmans WF, *et al*. Recommendations for standardized pathological characterization of residual disease for neoadjuvant clinical trials of breast cancer by the BIG-NABCG collaboration. *Ann Oncol*. 2015;**26**(7):1280–91.
6. Laas E, Labrosse J, Hamy AS, *et al*. Determination of breast cancer prognosis after neoadjuvant chemotherapy: comparison of Residual Cancer Burden (RCB) and Neo-Bioscore. *Br J Cancer*. 2021;**124**(8):1421–7.
7. Baker GM, King TA, Schnitt SJ. Evaluation of Breast and Axillary Lymph Node Specimens in Breast Cancer Patients Treated With Neoadjuvant Systemic Therapy. *Adv Anat Pathol*. 2019;**26**(4):221–34.
8. Luen SJ, Salgado R, Dieci MV, *et al*. Prognostic implications of residual disease tumor-infiltrating lymphocytes and residual cancer burden in triple-negative breast cancer patients after neoadjuvant chemotherapy. *Ann Oncol*. 2019;**30**(2):236–42.
9. Knauer M, Devries A, Wenzl E, *et al*. Standardization of pathologic complete response rates in breast cancer treatment. *Breast Cancer Res Treat*. 2008;**110**(2):395–6.
10. Mrkonjic M, Berman HK, Done SJ, *et al*. Breast specimen handling and reporting in the post-neoadjuvant setting: challenges and advances. *J Clin Pathol*. 2019;**72**(2):120–32.
11. Lanjewar S, Patil P, Fineberg S. Pathologic reporting practices for breast cancer specimens after neoadjuvant chemotherapy—a survey of pathologists in academic institutions across the United States. *Mod Pathol*. 2020;**33**(1):91–8.
12. Zhang M, Ma Y, Geng C, *et al*. Assisted computer and imaging system improve accuracy of breast tumor size assessment after neoadjuvant chemotherapy. *Transl Cancer Res*. 2021;**10**(3):1346–57.

13. Patel BK, Ranjbar S, Wu T, *et al.* Computer-aided diagnosis of contrast-enhanced spectral mammography: A feasibility study. *Eur J Radiol.* 2018;**98**:207–13.
14. Kennedy KM, Chin L, McLaughlin RA, *et al.* Quantitative micro-elastography: imaging of tissue elasticity using compression optical coherence elastography. *Sci Rep.* 2015;**5**:15538.
15. Brem RF, Lenihan MJ, Lieberman J, *et al.* Screening breast ultrasound: past, present, and future. *AJR Am J Roentgenol.* 2015;**204**(2):234–40.
16. Aboughaleb IH, Aref MH, El-Sharkawy YH. Hyperspectral imaging for diagnosis and detection of ex-vivo breast cancer. *Photodiagnosis Photodyn Ther.* 2020;**31**:101922.
17. Kho E, de Boer LL, Post AL, *et al.* Imaging depth variations in hyperspectral imaging: Development of a method to detect tumor up to the required tumor-free margin width. *J Biophotonics.* 2019;**12**(11):e201900086.
18. McCormack DR, Walsh AJ, Sit W, *et al.* In vivo hyperspectral imaging of microvessel response to trastuzumab treatment in breast cancer xenografts. *Biomed Opt Express.* 2014;**5**(7):2247–61.
19. Pradipta AR, Tanei T, Morimoto K, *et al.* Emerging Technologies for Real-Time Intraoperative Margin Assessment in Future Breast-Conserving Surgery. *Adv Sci (Weinh).* 2020;**7**(9):1901519.
20. Unger J, Hebisch C, Phipps JE, *et al.* Real-time diagnosis and visualization of tumor margins in excised breast specimens using fluorescence lifetime imaging and machine learning. *Biomed Opt Express.* 2020;**11**(3):1216–30.
21. Maloney BW, McClatchy DM, Pogue BW, *et al.* Review of methods for intraoperative margin detection for breast conserving surgery. *J Biomed Opt.* 2018;**23**(10):1–19.
22. Doyle TE, Factor RE, Ellefson CL, *et al.* High-frequency ultrasound for intraoperative margin assessments in breast conservation surgery: a feasibility study. *BMC Cancer.* 2011;**11**:444.
23. Sim YC, Ahn KM, Park JY, *et al.* Temperature-dependent terahertz imaging of excised oral malignant melanoma. *IEEE J Biomed Health Inform.* 2013;**17**(4):779–84.
24. Park JY, Choi HJ, Cheon H, *et al.* Terahertz imaging of metastatic lymph nodes using spectroscopic integration technique. *Biomed Opt Express.* 2017;**8**(2):1122–9.
25. Denis F, Desbiez-Bourcier AV, Chapiron C, *et al.* Contrast enhanced magnetic resonance imaging underestimates residual disease following neoadjuvant do cetaxel based chemotherapy for breast cancer. *Eur J Surg Oncol.* 2004;**30**(10):1069–76.
26. Maeda I, Kubota M, Ohta J, *et al.* Effectiveness of computer-aided diagnosis (CADx) of breast pathology using immunohistochemistry results of core needle biopsy samples for synaptophysin, oestrogen receptor and CK14/p63 for classification of epithelial proliferative lesions of the breast. *J Clin Pathol.* 2017;**70**(12):1057–62.
27. Hylton NM, Blume JD, Bernreuter WK, *et al.* Locally advanced breast cancer: MR imaging for prediction of response to neoadjuvant chemotherapy—results from ACRIN 6657/I-SPY TRIAL. *Radiology.* 2012;**263**(3):663–72.

28. Provenzano E, Bossuyt V, Viale G, *et al.* Standardization of pathologic evaluation and reporting of postneoadjuvant specimens in clinical trials of breast cancer: recommendations from an international working group. *Mod Pathol.* 2015;**28**(9):1185–201.
29. Board WCoTE. WHO Classification of Breast Tumours: WHO Classification of Tumours, Volume 2: World Health Organization; 2019.
30. Wang H, Mao X. Evaluation of the Efficacy of Neoadjuvant Chemotherapy for Breast Cancer. *Drug Des Devel Ther.* 2020;**14**:2423–33.
31. Rajan R, Esteva FJ, Symmans WF. Pathologic changes in breast cancer following neoadjuvant chemotherapy: implications for the assessment of response. *Clin Breast Cancer.* 2004;**5**(3):235–8.
32. Akbari H, Uto K, Kosugi Y, *et al.* Cancer detection using infrared hyperspectral imaging. *Cancer Sci.* 2011;**102**(4):852–7.
33. Hu Z, Fang C, Li B, *et al.* First-in-human liver-tumour surgery guided by multispectral fluorescence imaging in the visible and near-infrared-I/II windows. *Nat Biomed Eng.* 2020;**4**(3):259–71.
34. Halicek M, Fabelo H, Ortega S, *et al.* In-Vivo and Ex-Vivo Tissue Analysis through Hyperspectral Imaging Techniques: Revealing the Invisible Features of Cancer. *Cancers (Basel).* 2019;**11**(6).
35. Panasyuk SV, Yang S, Faller DV, *et al.* Medical hyperspectral imaging to facilitate residual tumor identification during surgery. *Cancer Biol Ther.* 2007;**6**(3):439–46.
36. Wang C, Zheng W, Bu Y, *et al.* Multi-scale hyperspectral imaging of cervical neoplasia. *Arch Gynecol Obstet.* 2016;**293**(6):1309–17.
37. Fei B, Lu G, Wang X, *et al.* Tumor margin assessment of surgical tissue specimen of cancer patients using label-free hyperspectral imaging. *Proc SPIE Int Soc Opt Eng.* 2017;**10054**.
38. Narimatsu T, Ozawa Y, Miyake S, *et al.* Biological effects of blocking blue and other visible light on the mouse retina. *Clin Exp Ophthalmol.* 2014;**42**(6):555–63.
39. Cakir M, Colak A, Calikoglu C, *et al.* Once the Light Touch to the Brain: Cytotoxic Effects of Low-Dose Gamma-Ray, Laser Light, and Visible Light on Rat Neuronal Cell Culture. *Eurasian J Med.* 2016;**48**(2):76–83.
40. Kohli I, Nahhas AF, Braunberger TL, *et al.* Spectral characteristics of visible light-induced pigmentation and visible light protection factor. *Photodermatol Photoimmunol Photomed.* 2019;**35**(6):393–9.
41. Dehrouyeh MH, Omid M, Ahmadi H, *et al.* Grading and Quality Inspection of Defected Eggs Using Machine Vision. *International Journal of Advance Science and Technology.* 2010;**16**:43–50.
42. Meriaudeau F, Ferraton M, Stolz C, *et al.* Polarization imaging for industrial inspection: SPIE; 2008.
43. Anderson RR. Polarized light examination and photography of the skin. *Arch Dermatol.* 1991;**127**(7):1000–5.
44. Reinhard E, Heidrich W, Debevec P, *et al.* High Dynamic Range Imaging: Acquisition, Display, and Image-Based Lighting: Elsevier Science; 2010.

45. Pastorello RG, Laws A, Grossmith S, *et al.* Clinico-pathologic predictors of patterns of residual disease following neoadjuvant chemotherapy for breast cancer. *Mod Pathol.* 2021;**34**(5):875–82.
46. Fushimi A, Kudo R, Takeyama H. Do Decreased Breast Microcalcifications After Neoadjuvant Chemotherapy Predict Pathologic Complete Response? *Clin Breast Cancer.* 2020;**20**(1):e82-e8.
47. Mieog JS, van de Velde CJ. Neoadjuvant chemotherapy for early breast cancer. *Expert Opin Pharmacother.* 2009;**10**(9):1423–34

Figures

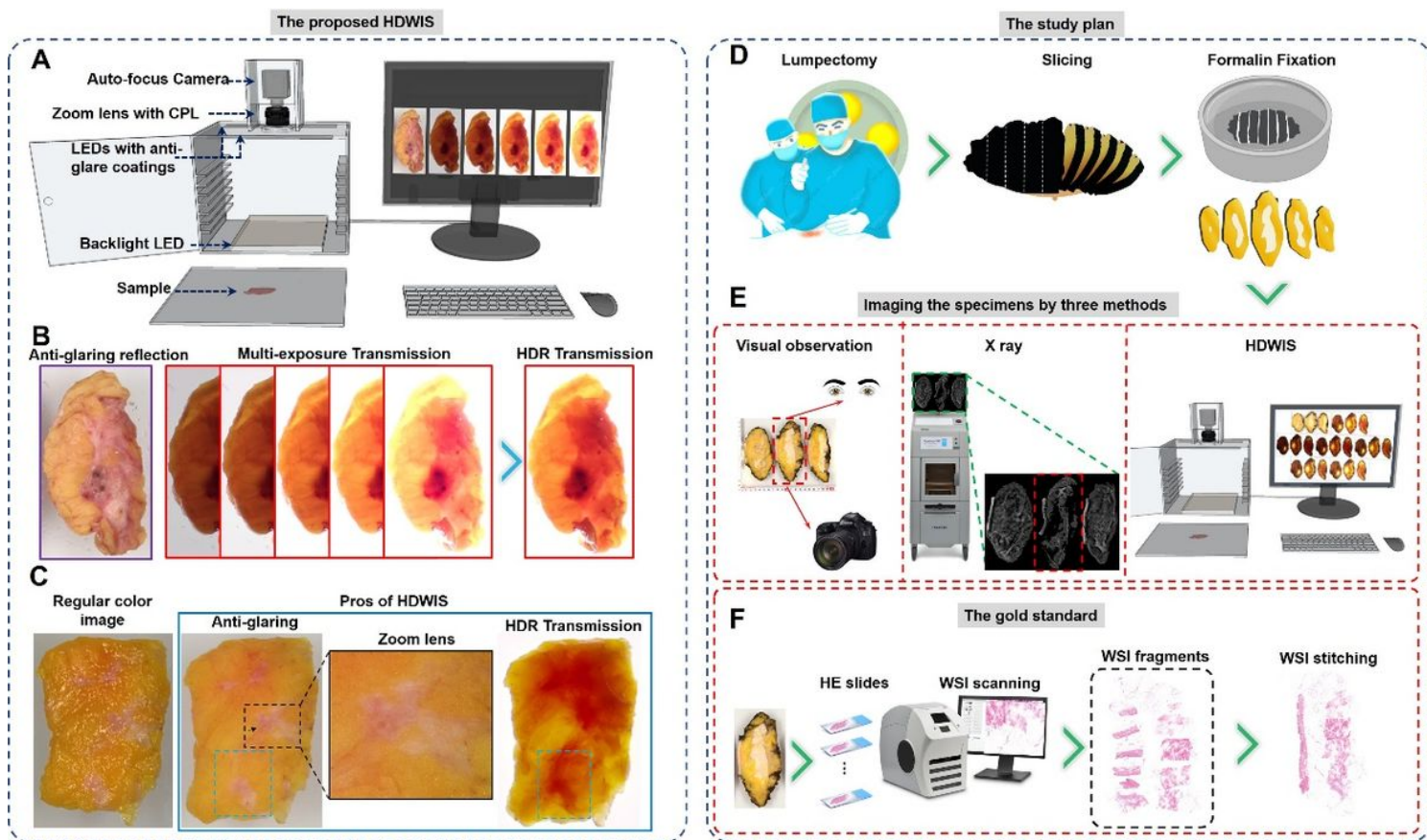


Figure 1

The schematic diagram and output of HDWIS and the study plan. A. The schematic diagram of HDWIS. B. Photos taken by HDWIS: one anti-reflective image and five transmission images with different exposures. An extra HDR image was composed using the transmission images. C. Compared with regular color images, HDWIS had three advantages: glare removal function, optical zooming, and transmission imaging. D. The specimen was dissected and fixed with 10% neutral formalin. E. Fibrosis and tumor areas were recorded and labeled by three methods. F. The slide which was stitched by WSI fragments was served as the gold standard to identify the tissue types in the specimen.

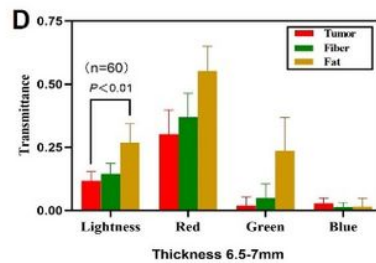
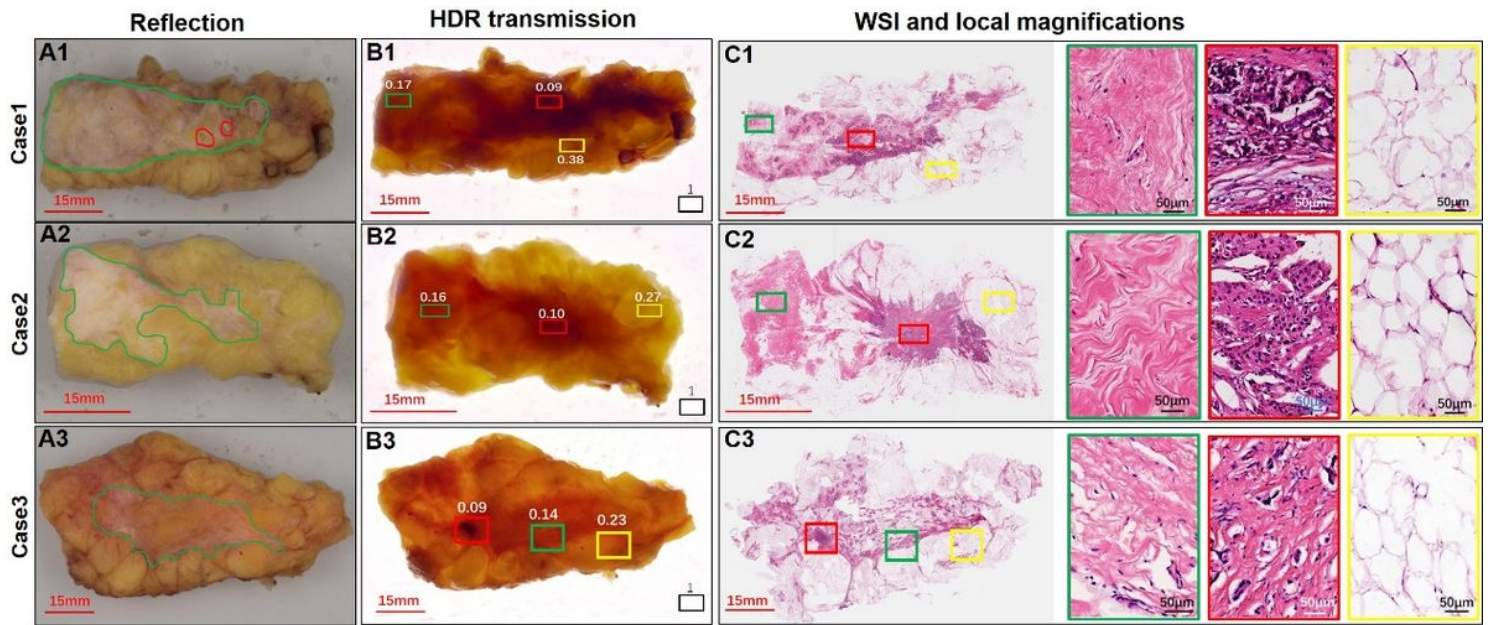


Figure 2

The differential transmittance of samples and the statistics analysis in transmittance for different components. A1-3. The reflection images of three breast cancer specimens. The green and red contour lines indicated the boundaries of fiber and tumor. B1-3. The HDR transmission images. The average brightness values of the region of interests were on top of these boxes. The brightness values were normalized to 0-1 with 1 indicating the brightness of the background (air). C1-3. The corresponding stitched WSI images with yellow, green, and red boxes indicating fat, fiber and tumor respectively. Zoom-in images of the box-indicated areas are provided on the right with corresponding box outline color. D. The average brightness of tumor, fat, and fiber from the transmission images of all 60 specimens. The light intensity of red, green, and blue channels was also demonstrated.

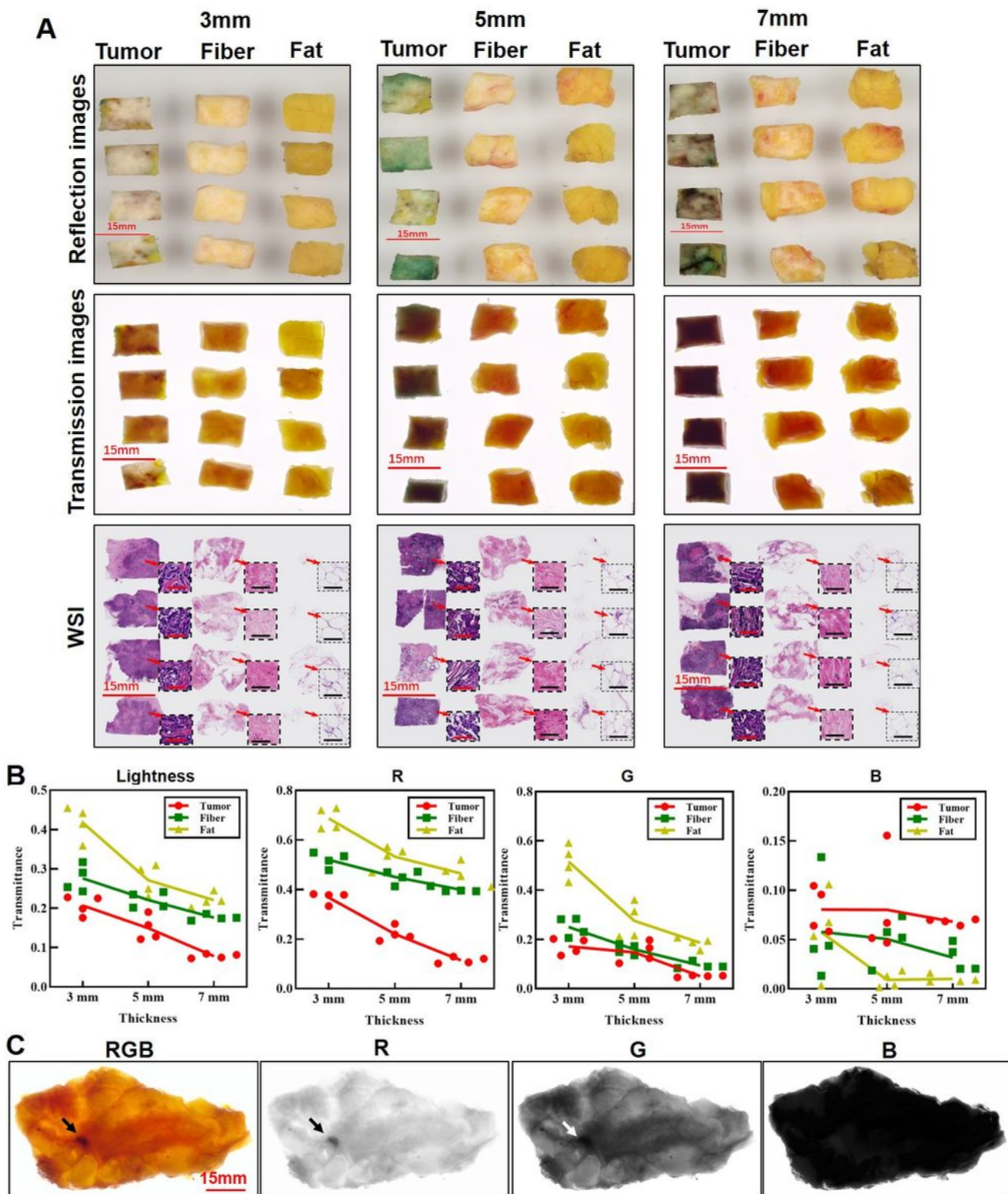


Figure 3

Matrix experiment and the application of transmittance. A. The reflection, transmission, and WSI of the 12 small tumor, fiber, and fat samples with a thickness of 3mm, 5mm and 7mm, respectively. Scale bars in the magnified WSI images denote 50 μ m. B. The average transmittance signal in different tissues with different thicknesses. WSI helped to select the region of interest for this calculation. C. The RGB in case 3 was divided to 3 channels. The suspicious small tumor area (arrow) with poor signal had similar value on

the curves of the tumor as shown in 3B except channel (B). This area was confirmed as tumor by the graphs.

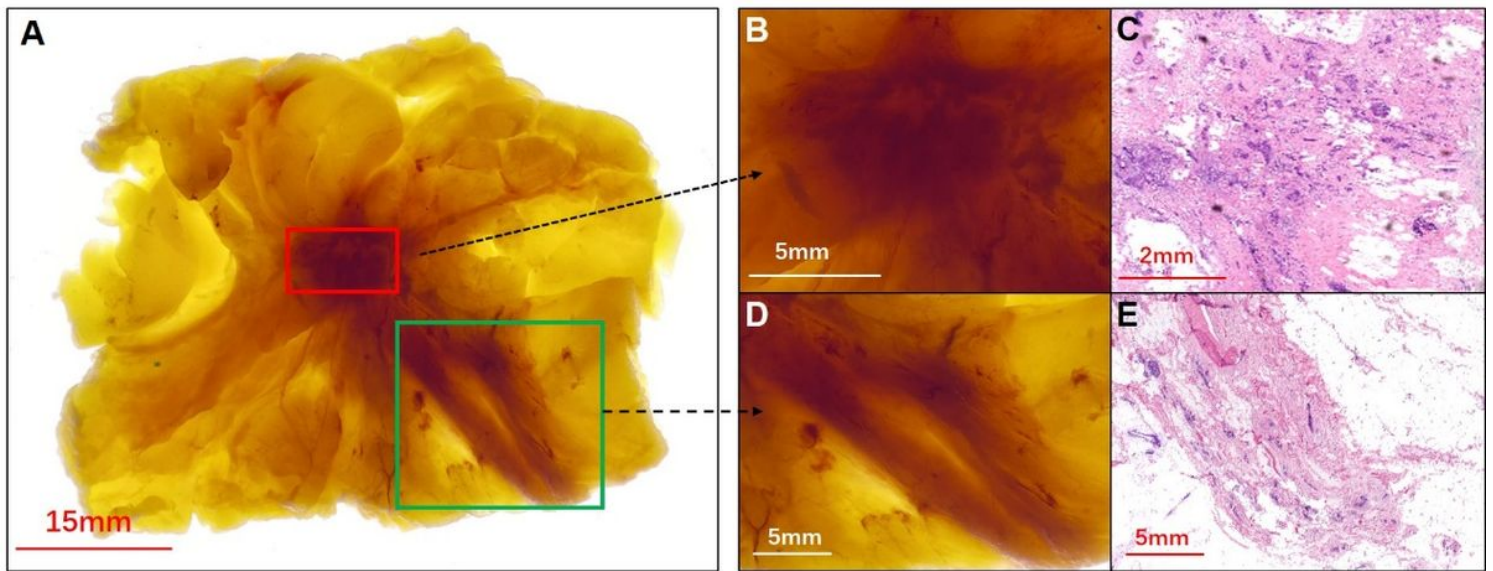


Figure 4

The texture of tumors and fibers in HDR. A. The red and green boxes indicated the tumor and fiber area of a breast cancer specimen. B1. Zoom-in transmission image of the tumor area. B2. Corresponding WSI of B1. C1. Zoom-in transmission image of the fiber area. C2. Corresponding WSI of C1.

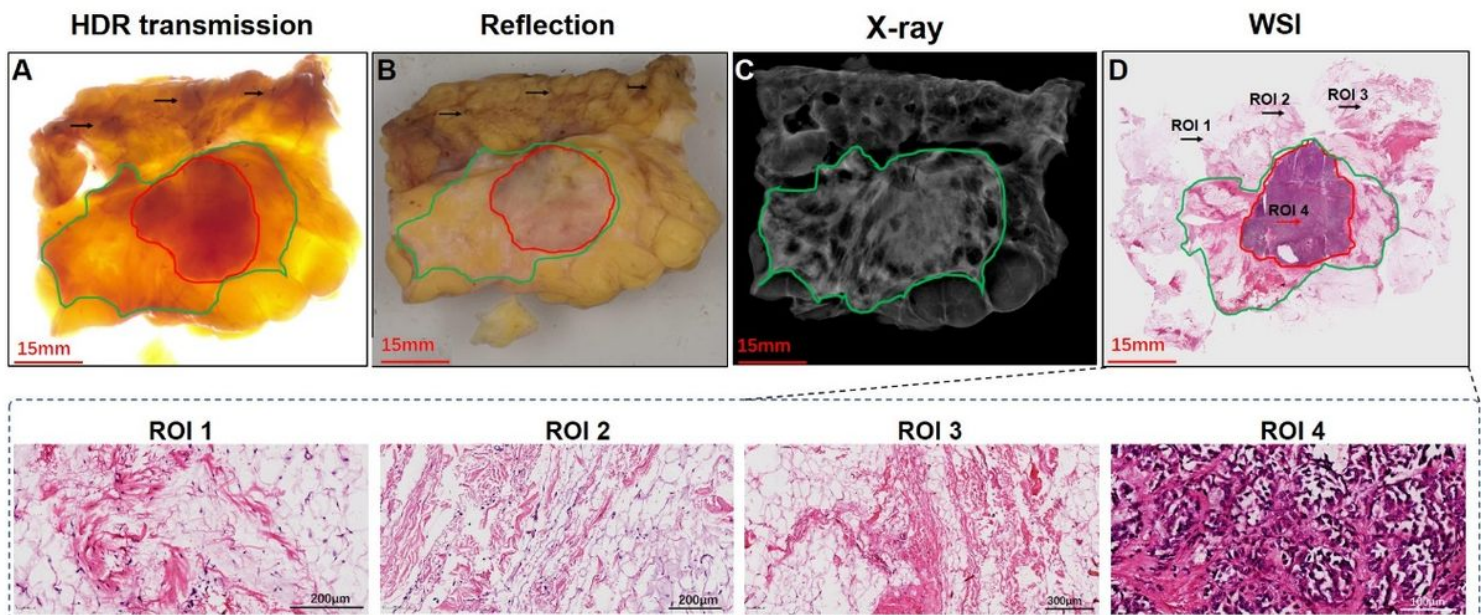
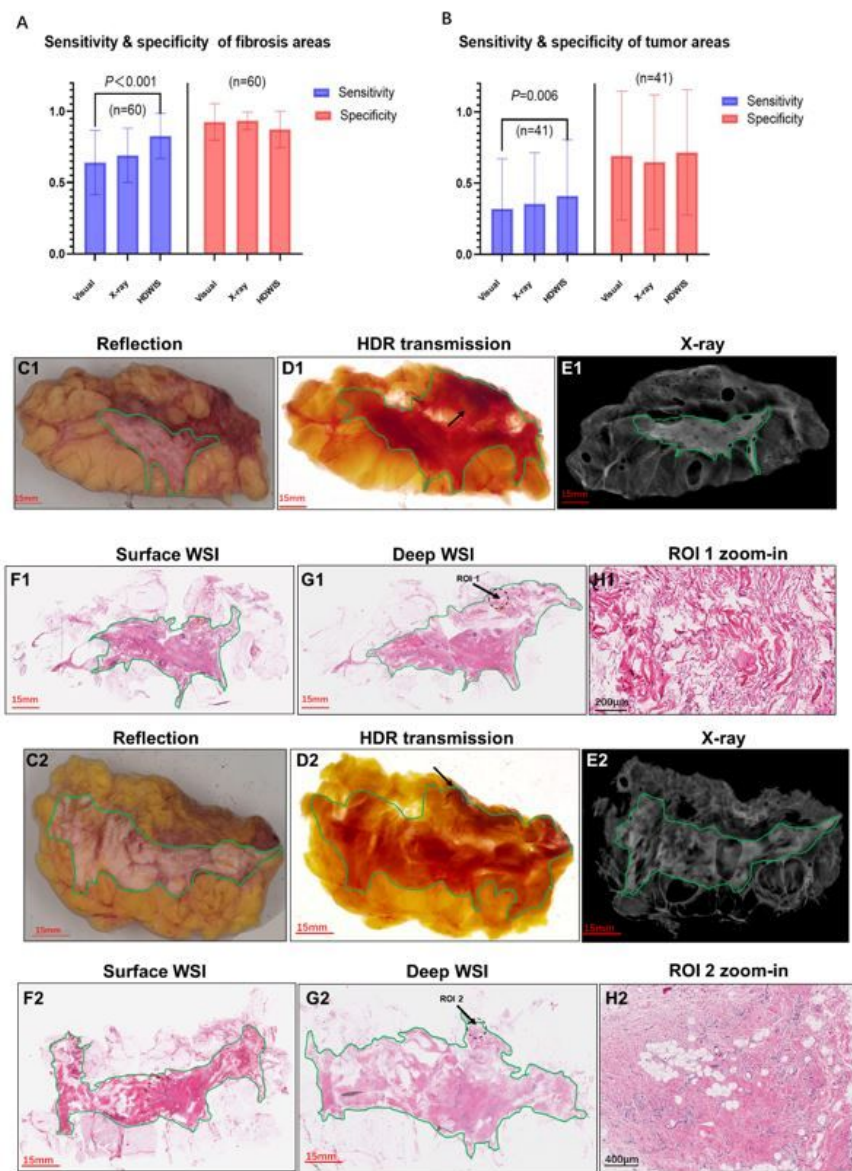


Figure 5

The reflection images helped eliminate the interference produced by transmission images. A1. The HDR showed two large tumor and fibrosis areas (red and green lines) and three small suspicious areas of tumor with poor transmittance indicated by black arrows. B. The reflection image showed the suspicious

grayish yellow areas as fats. C. The X-ray image showed high transmittance in fat but could not distinguish tumor from fibrosis. D. The WSI proved that the suspicious areas (arrows) were not tumors but fats mixed with a small percentage of fibers. The zoom-in images of black and red arrow indicated areas (ROI 1-4) are provided on the bottom of D.



The sensitivity and specificity of visual, X-ray and HDWIS for fibrosis areas location before and after deep cutting

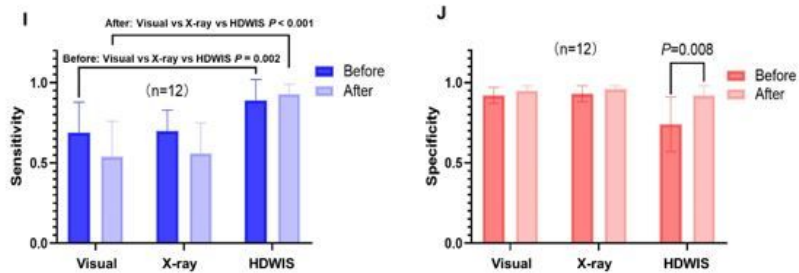


Figure 6

The sensitivity and specificity of visual observation and, X-ray, and HDWIS. A. The sensitivity of HDWIS was higher than that of X-ray and visual observation for fibrosis detection while the specificity was the lowest. B. HDWIS had the highest sensitivity for tumor detection and comparable specificity with the other two methods.

C1-H1, C2-H2. The HDR transmission images from two cases showed more complete fibrosis areas (arrows in D1 and D2) than that of original WSI (F1 and F2). These extra fibrosis areas were confirmed after deep sectioning (G1 and G2). The zoom-in images of ROI 1 and ROI 2 in G1 and G2 are provided in H1 and H2. It is difficult to identify the arrow-indicated fibrosis areas from the reflection (C1 and C2) and X-ray images (E1 and E2). I. After deep sectioning and reevaluation, the 12 cases which showed the larger fibrosis areas in HDWIS's transmission images had increased fiber sensitivity (before: 90%, after: 93.7%), while the visual observation and x-ray methods showed lower sensitivity than before. HDWIS had the highest fiber sensitivity among the three methods. J. HDWIS showed increased fiber specificity after deep sectioning (before: 74.5%, after: 92.9%).